# Quantum measurement and real-time feedback of a spin register in diamond

# Quantum measurement and real-time feedback

# of a spin register in diamond

**Proefschrift**

ter verkrijging van de graad van doctor
aan de Technische Universtiteit Delft,
op gezag van de Rector Magnificus Prof. ir. K.C.A.M. Luyben,
voorzitter van het College voor Promoties,
in het openbaar te verdedigen op om uur

door


**Machiel BLOK**

MSc
geboren te Amsterdam, Netherlands

*Dit proefschrift is goedgekeurd door de promotor:*
Prof. dr. ir. R. Hanson

*Samenstelling promotiecommissie:*

| | |
|---|---|
| Rector Magnificus, | voorzitter |
| Prof. dr. ir. R. Hanson, | Technische Universiteit Delft, promotor |



ISBN

Casimir PhD Series Delft-Leiden 2013-36

Cover design: L.D. Swakman

Printed by Gildeprint Drukkerijen — www.gildeprint.nl

An electronic version of this thesis is available at www.library.tudelft.nl/dissertations

# Contents

Chapter 1

# Introduction

M.S. Blok

Chapter 2

# Theoretical Background

M.S. Blok

## 2.1 NV-center in diamond

### 2.1.1 Optical level structure

### 2.1.2 Ground state level structure

### 2.1.3 Coupling to nuclear spins

## 2.2 Quantum measurements

### 2.2.1 Von Neaumann picture

### 2.2.2 Projection operator

### 2.2.3 Measurements as a tool for quantum information

### 2.2.4 The measurement problem

Chapter 3

# Experimental methods

M.S. Blok

## 3.1 Samples and fabrication

### 3.1.1 Localization

### 3.1.2 SILs

### 3.1.3 Anti reflection coating

## 3.2 Setup

## 3.3 Optical initialisation and readout of electron spin

## 3.4 Electron and nuclear spin manipulation

## 3.5 Real-time feedback

Chapter 4

# Manipulating a qubit through the backaction of sequential partial measurements and real-time feedback

M.S. Blok, C. Bonato, M.L. Markham, D.J. Twitchen, V.V. Dobrovitski and R. Hanson

Quantum measurements not only extract information from a system but also alter its state. Although the outcome of the measurement is probabilistic, the backaction imparted on the measured system is accurately described by quantum theory [1,2,3]. Therefore, quantum measurements can be exploited for manipulating quantum systems without the need for control fields [4,5]. We demonstrate measurement-only state manipulation on a nuclear spin qubit in diamond by adaptive partial measurements. We implement the partial measurement via tunable correlation with an electron ancilla qubit and subsequent ancilla readout [6,7]. We vary the measurement strength to observe controlled wavefunction collapse and find post-selected quantum weak values [6,7,8,9,10]. By combining a novel quantum non-demolition readout on the ancilla with real-time adaption of the measurement strength we realize steering of the nuclear spin to a target state by measurements alone. Besides being of fundamental interest, adaptive measurements can improve metrology applications [11,12] and are key to measurement-based quantum computing [13,14].

This chapter has been published in *Nature Physics* **10**, 189-193 (2014).

## 4.1 Introduction

Measurements play a unique role in quantum mechanics and in quantum information processing. The backaction of a measurement can be used for state initialization[15,16], generation of entanglement between non-interacting systems[17,18,19,20], and for qubit error detection[21]. These measurement-based applications require either post-selection or real-time feedback, as the outcome of a measurement is inherently probabilistic. Recent experiments achieved quantum feedback control on a single quantum system[20,22,23,24] by performing coherent control operations conditioned on a measurement outcome.

Here, we realize real-time adaptive measurements and exploit these in a proof-of-principle demonstration of measurement-only quantum feedback. Our protocol makes use of partial measurements that balance the information gain and the measurement backaction by varying the measurement strength. We accurately control the measurement strength and the corresponding backaction in a two-qubit system by tuning the amount of (quantum) correlation between the system qubit and an ancilla qubit, followed by projective readout of the ancilla[6,7]. In general, the backaction of sequential partial measurements leads to a random walk[1,2,3] but by incorporating feedback, multiple measurements can direct the trajectory of a qubit towards a desired state[4,5]. Real-time adaptive measurements are a key ingredient for quantum protocols such as one-way quantum computing[13,14] and Heisenberg-limited phase estimation[11,12].

We implement the adaptive partial measurements in a nitrogen vacancy (NV) center in synthetic diamond. We define the system qubit by the nuclear spin of the NV host nitrogen ($|\downarrow\rangle$: $m_I$=0, $|\uparrow\rangle$: $m_I$= -1), and the ancilla qubit by the NV electron spin ($|0\rangle$: $m_S$=0, $|1\rangle$: $m_S$=-1) (Fig. 4.1a). The ancilla is initialized and read out in a single shot with high fidelity using spin-selective optical transitions[15]. We perform single-qubit operations on the ancilla by applying microwave frequency pulses to an on-chip stripline.

## 4.2 Variable-strength measurement

We realize the variable-strength measurement by correlating the system qubit with the ancilla through a controlled-phase-type gate (Fig. 4.1b) that exploits the hyperfine interaction, which (neglecting small off-diagonal terms) has the form $\hat{H}_{hf} = A\hat{S}_z\hat{I}_z$ (with $A = 2\pi \times 2.184 \pm 0.002$ MHz and $\hat{S}_z, \hat{I}_z$ the three-level Pauli z-operators for the electron, nuclear spin respectively). During free evolution, the ancilla qubit precession is conditional on the state of the system qubit. We choose the rotating frame such that the ancilla rotates clockwise (anti-clockwise) around the z-axis if the system qubit is in $|\uparrow\rangle$ ($|\downarrow\rangle$) and vary the interaction time $\tau$. For $\tau = 0$, there is no correlation between the ancilla and the system, whereas for $\tau = \frac{\pi}{A}$, corresponding to the rotation angle $\theta = 90°$, the two are maximally correlated. A subsequent rotation and projective readout of the ancilla then implements a measurement of the system qubit, with a measurement strength that can be accurately

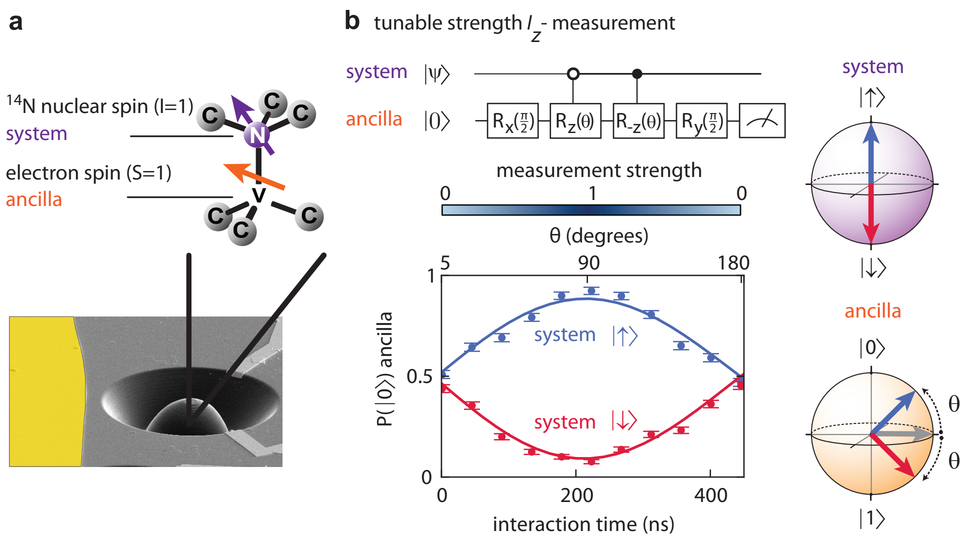


**Figure 4.1 | Partial measurement of a spin qubit in diamond.** (a) The NV center is a natural two-qubit system where the system qubit is defined by the $^{14}N$ nuclear spin and the ancilla qubit is defined by the electron spin. A solid-immersion-lens is deterministically fabricated on top of the selected NV center to increase the photon collection efficiency. Control fields for single qubit rotations are generated by applying a current to the gold stripline (yellow). (b) A tunable strength measurement is implemented by a Ramsey-type gate on the ancilla. We plot the probability to measure the state $|0\rangle$ for the ancilla, as a function of interaction time $\tau$, for two system input states $|\downarrow\rangle$ (red) and $|\uparrow\rangle$ (blue). The Bloch-spheres show the state of the system (purple) and ancilla (orange) after the entangling-gate for the different input states (red and blue vectors). The colour bar represents the measurement strength, proportional to $\sin\theta$, where $\theta = \frac{A\tau}{2}$. Blue corresponds to a projective measurement and white to no measurement. Solid lines are a fit to the function $y_0 + e^{-(\frac{\tau}{T_2^*})^2}\cos(A\tau + \delta)$. From the phase offset $\delta$ we find the weakest measurement we can perform, corresponding to $\theta = 5°$. This is limited by free evolution of the ancilla during the pulses.(see !!!TODO REFERENCE SOM!!!). Error bars depict 68 $\%$ confidence intervals. Sample size is 500 for each data point.

tuned by controlling the interaction time $\tau$. A mathematical derivation can be found in the !!! TODO: REFERENCE TO SOM!!!

We investigate the measurement-induced backaction by preparing an initial state of the system ($|\uparrow\rangle$ , $|x\rangle$ and $|y\rangle$) and performing a partial measurement with strength $\theta$, followed by state tomography (Fig. 4.2a). First, we neglect the outcome of the partial measurement, which is mathematically equivalent to taking the trace over the state of the ancilla qubit. In this case the backaction is equivalent to pure dephasing as can be seen by a measured reduction of the length of the Bloch vector (Fig. 4.2b). Next, we condition the tomography on the ancilla measurement yielding state $|0\rangle$ (Fig. 4.2c). We observe that for a weak measurement ($\theta = 5^\circ$), the system is almost unaffected, whereas for increasing measurement strength it receives a stronger kick towards $|\uparrow\rangle$(Fig. 4.2c). Crucially, we find that the length of the Bloch vector is preserved in this process, as expected for an initially pure state. This shows that the partial collapse is equivalent to a qubit rotation that is conditional on the measurement strength and outcome and on the initial state. By performing quantum process tomography, we find that both measurement processes agree well with the theoretical prediction (the process fidelities are $0.986 \pm 0.004$ and $0.94 \pm 0.01$ for the unconditional and conditional process, respectively; see !!!TO REFERENCE TO SOM!!!).

## 4.3 Generalized weak value

By combining a partial measurement with post-selection on the outcome of a subsequent projective measurement, we can measure the generalized weak value $_f\langle I_z\rangle$ (conditioned average of contextual values[25], see !!TODO ADD REF TO SOM!!!) of the nuclear spin in the $z$-basis. In the limit of zero measurement strength ($\theta = 0^\circ$), this quantity approximates the weak value[8] $W = \frac{\langle\psi_f|\hat{I}_z|\psi_i\rangle}{\langle\psi_f|\psi_i\rangle}$ , where $\psi_i(\psi_f)$ is the initial (final) state of the nucleus and from here we define $\hat{I}_z$ as the Pauli $z$-operator reduced to a two-level system with eigenvalues +1 and $-1$. By post-selecting only on the final states having small overlap with the initial state, $_f\langle I_z\rangle$ can be greatly amplified to values that lie outside the range of eigenvalues of the measured observable. As shown in Fig. 4.3, by sweeping the angle between the initial and final states we observe up to tenfold amplification ($_f\langle I_z\rangle = 10 \pm 3$) compared to the maximum eigenvalue of $I_z$ ($+1$). This amplification is the highest reported for a solid-state system to date[7]. As predicted[26], we observe that values of $_f\langle I_z\rangle$ lying outside of the range of eigenvalues of $I_z$ can be found for any finite measurement strength.

## 4.4 QND-measurement of the ancilla qubit

Using the partial measurements for measurement-based feedback requires reading out the ancilla without perturbing the system qubit. In our experiment the system qubit can dephase during ancilla readout both through a spin-flip of the electron in the course of optical

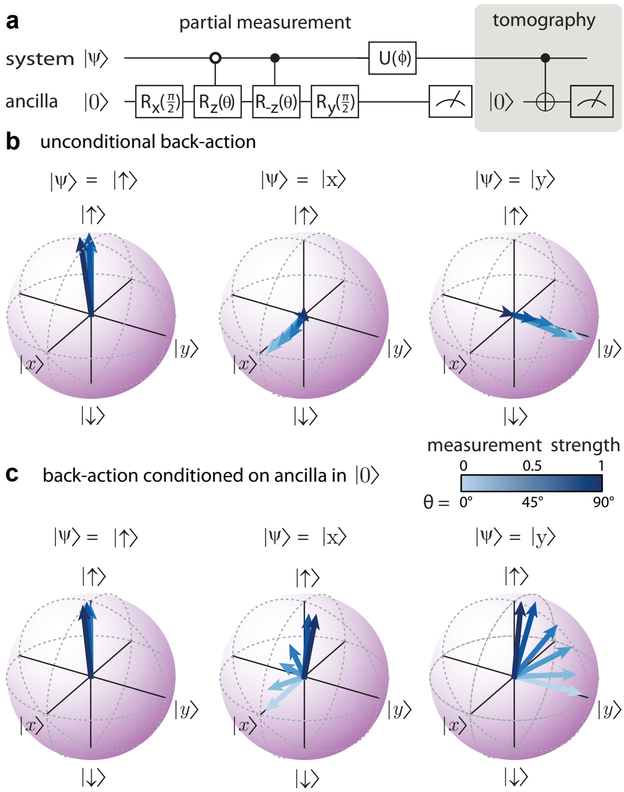


**Figure 4.2 | Measurement backaction for variable-strength measurement.** (a) We prepare an initial state of the system ($|\uparrow\rangle$, $|x\rangle$ and $|y\rangle$), perform a partial measurement with strength $\theta$, and characterize the measurement backaction on the system by quantum state tomography. Quantum state tomography is implemented by an ancilla-assisted projective measurement, performed with the same protocol, setting $\tau = 229$ ns for $\theta = 90°$. The nuclear spin basis rotation is performed with a $\frac{\pi}{2}$ radio-frequency pulse (along either $x$ or $y$). The basis rotation pulse for the tomography is applied before the readout of the ancilla, to avoid the dephasing induced by the state-characterization measurement (see main text). The data is corrected for errors in the readout and initialization of the system qubit, both of which are obtained from independent measurements (see !!! TODO REFERENCE SOM!!!). (b,c) Measurement backaction for a partial measurement of increasing strength, independent of the measurement result for the ancilla qubit (b), or conditioned on the ancilla in $|0\rangle$ (c).

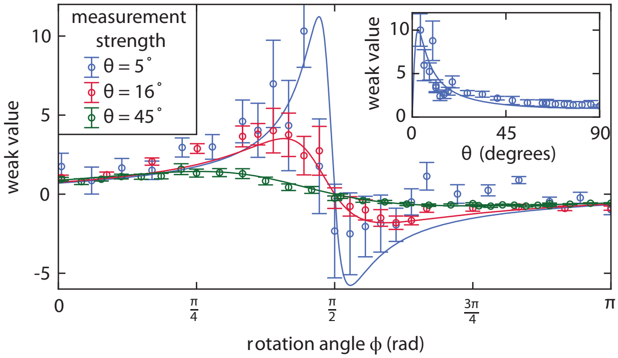


**Figure 4.3 | Generalized quantum weak value**. Measurement of a generalized weak value for the nuclear-spin qubit, performed by a partial measurement of strength $\theta$, followed by a strong measurement and post-selection of the state $|\downarrow\rangle$, as a function of the basis rotation angle $\phi$ of the strong measurement (Fig. 4.2a). Solid lines are simulations using independently determined parameters. The asymmetry in the curve can be explained by asymmetric nuclear spin flips arising during ancilla initialisation by optical excitation of the forbidden transition of $E_y$ (see !!TODO REFERENCE SOM!!). Inset: the generalized weak values as a function of the strength $\theta$ of the partial measurement, setting the basis rotation angle of the strong measurement to the optimal value $\phi = \frac{\pi}{2} - \theta$. All error bars depict 68 % confidence intervals. The sample size varies per data point because each data point has different post-selection criterion.

excitation (Fig. 4.4b) and as a result of the difference in the effective nuclear g-factor in the electronic ground- and optically excited state[27]. Note that for the characterization of a single partial measurement (Fig. 4.2) we circumvent this dephasing by interchanging the measurement basis rotation and the ancilla readout; this interchange is not possible for real-time adaptive measurements.

To mitigate the nuclear dephasing during ancilla readout we reduce the ancilla spin-flip probability using a dynamical-stop readout technique. We partition the optical excitation time in short (1 $\mu$s) intervals and we stop the excitation laser as soon as a photon is detected, or after a predetermined maximum readout time when no photon is detected (Fig. 4.4a). This reduces redundant excitations without compromising the readout fidelity. In Fig. 4.4b we show the correspondence between pre- and post-measurement states for the two eigenstates of the ancilla. For the state $|0\rangle$ the dynamical-stop readout increases the fidelity ($F = \langle\psi_i|\rho_m|\psi_i\rangle$, where $\rho_m$ is the density matrix of the system after the ankle readout) from $0.18 \pm 0.02$ to $0.86 \pm 0.02$. The latter fidelity is solely limited by the cases

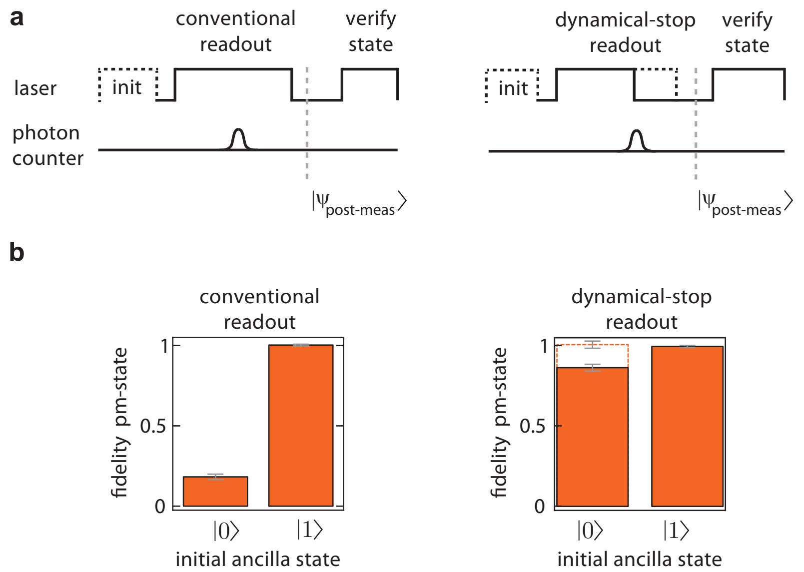


**Figure 4.4 | Quantum non-demolition measurement of the ancilla qubit** (a) The ancilla is initialized in $|0\rangle$ ($|1\rangle$) by optically pumping the $A_2$ ($E_y$) transition. The ancilla is then read out by exciting the $E_y$ transition for 100 $\mu$s (conventional readout), or until a photon was detected (dynamical-stop readout). Finally, we verify the post-measurement state with a conventional readout. (b) Fidelity of the post-measurement state of the ancilla for conventional readout (left graph) and dynamical-stop readout (right graph). Results are corrected for the infidelity in the final readout. All error bars depict 68 $\%$ confidence intervals. Sample size per datapoint is 5000

where the spin flipped before a photon was detected: we find $F = 1.00 \pm 0.02$ for the cases in which a photon was detected. As expected, the fidelity is high ($F = 0.996 \pm 0.006$) for input state $|1\rangle$ as this state is unaffected by the excitation laser. The dynamical-stop technique thus implements a quantum non-demolition (QND) measurement of the ancilla electron spin with an average fidelity of $0.93 \pm 0.01$ for the post-measurement state.

The dynamical-stop readout of the ancilla significantly reduces the dephasing of the nuclear spin qubit during measurement as shown in Fig. 4.5. Starting with the nuclear spin in state $|x\rangle = \frac{|0\rangle+|1\rangle}{\sqrt{2}}$, a conventional readout of the ancilla completely dephases the nuclear spin, leading to a state fidelity with respect to $|x\rangle$ of 0.5. In contrast, the fidelity of the dynamical-stop readout saturates to $0.615 \pm 0.002$ (probably limited by changes in the effective g-factor of the nuclear spin). The dynamical-stop readout thus leaves the system in a coherent post-measurement state that can be used in a real-time feedback protocol.

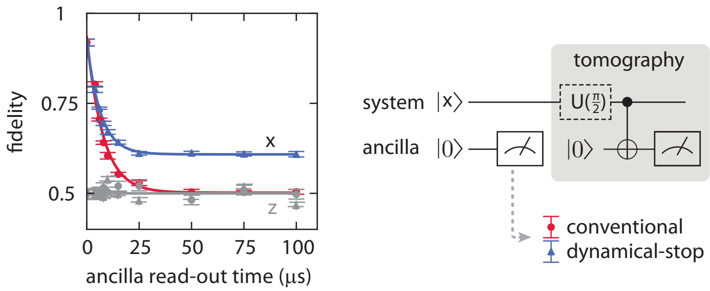


**Figure 4.5 | System qubit coherence during ancilla readout**. Coherence of the system qubit state after ancilla readout. For the dynamical-stop protocol we define the ancilla readout time as the predetermined maximum readout time. The graph shows the fidelity of the system with respect to $|x\rangle$ for conventional readout (red) and dynamical-stop readout (blue). The $z$-component of the system is unaffected as shown by the constant fidelity with respect to $|\uparrow\rangle$ (grey). All error bars depict 68 $\%$ confidence intervals. Sample size per datapoint is 2000

## 4.5 Control by adaptive measurements

Preserving coherence of the post-measurement state enables a proof-of-principle realization of measurement-only control, by implementing sequential measurements and tuning the strength of the second measurement in real time conditioned on the outcome of the first measurement (Fig. 4.6a). We choose as our target the creation of the state $|\psi\rangle = \cos\left(\frac{\pi}{4} + \frac{\theta_1}{2}\right)|\downarrow\rangle + \cos\left(\frac{\pi}{4} - \frac{\theta_1}{2}\right)|\uparrow\rangle$ from initial state $|x\rangle$ using only partial measurements of $\hat{I}_z$. The first measurement with strength $\theta_1$ will prepare either the desired state, or the state $|\psi_{wrong}\rangle = \cos\left(\frac{\pi}{4} - \frac{\theta_1}{2}\right)|\downarrow\rangle + \cos\left(\frac{\pi}{4} + \frac{\theta_1}{2}\right)|\uparrow\rangle$ , each with probability 0.5. We adapt the strength of the second measurement $\theta_2$ according to the outcome of the first measurement: we set $\theta_2 = 0$ if the first measurement directly yielded the target state, but if the wrong outcome was obtained we set the measurement strength to

$$\theta_2 = \sin^{-1}\left[2\frac{\sin\theta_1}{1+\sin^2\theta_1}\right], \tag{4.1}$$

such that the second measurement will probabilistically rotate the qubit to the target state (see !!!TODO REF to sup!!!). The total success probability of this two-step protocol is $p_{suc} = \frac{1}{2}(1+\cos\theta_1)$ and a successful event is heralded by the outcome of the ankle readout. In principle the protocol can be made fully deterministic[4] by incorporating a reset in the form of a projective measurement along the $x$-axis.

To find the improvement achieved by the feedback, we first compare the success probability of our adaptive measurement protocol to the success probability for a single measurement

(Fig. 4.6b right panel). The success probability clearly increases with the adaptive protocol and is proportional to the readout fidelity of the $|0\rangle$ state of the ancilla, which is maximum for readout times > 25 $\mu$s. The fidelity of the final state (Fig. 4.6b left panel) is limited by the remaining dephasing of the system during readout of the ancilla as shown in Fig. 4.5. This constitutes the trade-off between success probability and state fidelity.

We show that the increase in success probability is non-trivial by comparing the final state fidelity with and without feedback (Fig. 4.6b left panel). In principle the success probability can be increased in the absence of feedback by accepting a certain number of false measurement outcomes at the cost of a reduced fidelity. We calculate the maximum fidelity that can be achieved in this way by performing only the first measurement and increasing the success probability to that of the adaptive protocol using post-selection (grey line in Fig. 4.6b, left panel). We find that the measured state fidelity in the adaptive protocol is above this bound (Fig. 4.6b, green area), which indicates that the adaptive measurement indeed successfully corrects the kickback from the first measurement, thus yielding a clear advantage over open-loop protocols.

We note that, in contrast to pioneering adaptive measurement experiments on photons that only used experimental runs in which a photon was detected at each measurement stage [14], our protocol is fully deterministic in the sense that the partial measurement always yields an answer. In particular, the data in Fig. 4.6 includes all experimental runs and thus no post-selection is performed, as desired for future applications in metrology and quantum computing.

The performance of the protocol can be further improved by increasing the ancilla readout fidelity (either by improving the collection efficiency or reducing spin-flip probability) and by further reducing the dephasing of the system during readout. A particularly promising route is to use nuclear spins farther away from the NV center (for example carbon-13 spins) that have much smaller hyperfine couplings [28,29,30] and are more robust against changes in the orbital state of the electron spin.

Our work is the first experimental exploration of a fundamental concept of control-free control [31,4,5] . Furthermore, the use of adaptive measurements as presented here can increase the performance of spin-based magnetometers [11,12]. Finally, our results can be combined with recently demonstrated methods for generating entanglement between separate nitrogen vacancy centre spins [32,33]. Taken together, these techniques form the core capability required for one-way quantum computing, where quantum algorithms are executed by sequential adaptive measurements on a large entangled 'cluster' state [13,14].

## 4.6 Methods

We use a naturally-occurring nitrogen-vacancy center in high-purity type IIa CVD diamond, with a <111>-crystal orientation obtained by cleaving and polishing a <100>-substrate.

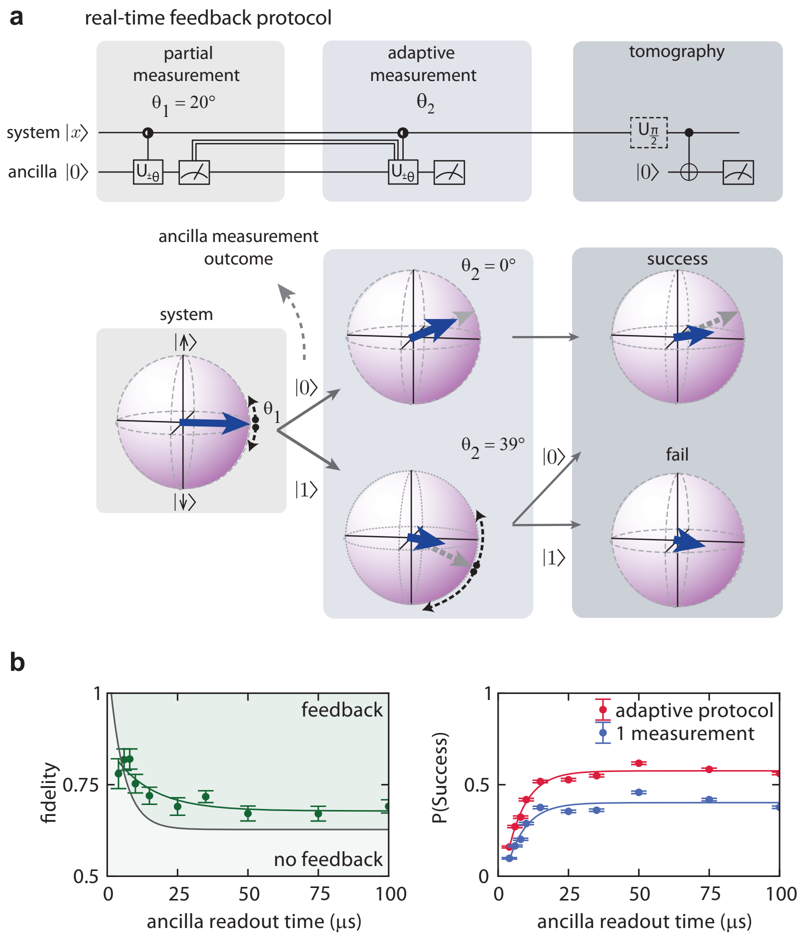


**Figure 4.6 | Manipulation of a nuclear spin state by sequential partial adaptive measurements with real-time feedback.** (a) Adaptive measurement protocol. The ancilla qubit is initialized in $|0\rangle$ and the system qubit is prepared in $|x\rangle$. The strength of the second measurement ($\theta_2$) is adjusted according to the outcome of the first measurement. The system is analysed by state tomography at each intermediate step. The result of the tomography is plotted on the bloch spheres (blue vector) and compared with the ideal case (grey vector). (b) Fidelity of the output state with respect to the target state as a function of ancilla readout time (dynamical-stop readout) with feedback (only the cases where the protocol heralds success). The grey line is obtained by performing one measurement and adding negative results to artificially increase the success probability to that of the adaptive protocol (red line in right panel). In the right panel we show the probability that the protocol heralds success for one measurement and for the adaptive protocol.

Experiments are performed in a bath cryostat, at the temperature of 4.2 K, with an applied magnetic field of 17 G. Working at low-temperature, we can perform efficient electron spin initialization (F = 0.983 $\pm$ 0.006) and single-shot readout (the fidelity is 0.853 $\pm$ 0.005 for $m_S = 0$ and 0.986 $\pm$ 0.002 for $m_S = -1$) by spin-resolved optical excitation[15]. Initialization of the nuclear spin is done by measurement[15], with fidelity 0.95 $\pm$ 0.02. Single-qubit operations can be performed with high accuracy using microwave (for the electron) and radio-frequency (for the nucleus) pulses applied to the gold stripline. Note that the single-qubit operations on the nucleus are only used for state preparation and tomography, but not in the feedback protocol. The dephasing time $T_2^*$ is (7.8 $\pm$ 0.2) ms for the nuclear spin and (1.35 $\pm$ 0.03) $\mu$s for the electron spin.

## 4.7 Bibliography


[1] C. Guerlin *et al.* Progressive field-state collapse and quantum non-demolition photon counting. *Nature* **448**, 889 (2007).

[2] M. Hatridge *et al.* Quantum Back-Action of an Individual Variable-Strength Measurement. *Science* **339**, 178 (2013).

[3] K. W. Murch, S. J. Weber, C. Macklin and I. Siddiqi. Observing single quantum trajectories of a superconducting quantum bit. *Nature* **502**, 211 (2013).

[4] S. Ashhab and F. Nori. Control-free control: Manipulating a quantum system using only a limited set of measurements. *Physical Review A* **82**, 062103 (2010).

[5] H. Wiseman. Quantum control: Squinting at quantum systems. *Nature* **470**, 178 (2011).

[6] T. Brun, L. Diósi and W. Strunz. Test of weak measurement on a two- or three-qubit computer. *Physical Review A* **77**, 032101 (2008).

[7] J. Groen *et al.* Partial-Measurement Backaction and Nonclassical Weak Values in a Superconducting Circuit. *Physical Review Letters* **111**, 090506 (2013).

[8] Y. Aharonov, D. Z. Albert and L. Vaidman. How the result of a measurement of a component of the spin of a spin-1/2 particle can turn out to be 100. *Physical Review Letters* **60**, 1351 (1988).

[9] G. Pryde, J. O'Brien, A. White, T. Ralph and H. Wiseman. Measurement of Quantum Weak Values of Photon Polarization. *Physical Review Letters* **94**, 220405 (2005).

[10] J. Dressel, M. Malik, F. M. Miatto, A. N. Jordan and R. W. Boyd. Understanding Quantum Weak Values: Basics and Applications. Preprint at http://arxiv.org/abs/1305.7154 (2013).

[11] P. Cappellaro. Spin-bath narrowing with adaptive parameter estimation. *Physical Review A* 030301(R)–5 (2012).

[12] B. L. Higgins, D. W. Berry, S. D. Bartlett, H. M. Wiseman and G. J. Pryde. Entanglement-free Heisenberg-limited phase estimation. *Nature* **450** (2007).

[13] R. Raussendorf and H. Briegel. A one-way quantum computer. *Physical Review Letters* **86**, 5188 (2001).

[14] R. Prevedel *et al.* High-speed linear optics quantum computing using active feed-forward. *Nature* **445**, 65 (2007).

[15] L. Robledo *et al.* High-fidelity projective read-out of a solid-state spin quantum register. *Nature* **477**, 574 (2011).

[16] D. Ristè, J. G. van Leeuwen, H.-S. Ku, K. W. Lehnert and L. DiCarlo. Initialization by measurement of a superconducting quantum bit circuit. *Physical Review Letters* **109**, 050507 (2012).

[17] C. W. Chou *et al.* Measurement-induced entanglement for excitation stored in remote atomic ensembles. *Nature* **438**, 828 (2005).

[18] D. L. Moehring *et al.* Entanglement of single-atom quantum bits at a distance. *Nature* **449**, 68 (2007).

[19] W. Pfaff *et al.* Demonstration of entanglement-by-measurement of solid-state qubits. *Nature Physics* 29–33 (2012).

[20] D. Ristè *et al.* Deterministic entanglement of superconducting qubits by parity measurement and feedback. *Nature* **502**, 350 (2013).

[21] J. Chiaverini *et al.* Realization of quantum error correction. *Nature* **432**, 602 (2004).

[22] G. G. Gillett *et al.* Experimental Feedback Control of Quantum Systems Using Weak Measurements. *Physical Review Letters* **104**, 080503 (2010).

[23] C. Sayrin *et al.* Real-time quantum feedback prepares and stabilizes photon number states. *Nature* **477**, 73 (2011).

[24] R. Vijay *et al.* Stabilizing Rabi oscillations in a superconducting qubit using quantum feedback. *Nature* **490**, 77 (2012).

[25] J. Dressel, S. Agarwal and A. N. Jordan. Contextual values of observables in quantum measurements. *Physical Review Letters* **104**, 240401 (2010).

[26] N. S. Williams and A. N. Jordan. Weak values and the Leggett-Garg inequality in solid-state qubits. *Physical Review Letters* **100**, 026804 (2008).

[27] L. Jiang *et al.* Coherence of an Optically Illuminated Single Nuclear Spin Qubit. *Physical Review Letters* **100**, 073001 (2008).

[28] N. Zhao *et al.* Sensing single remote nuclear spins. *Nature nanotechnology* **7**, 657 (2012).

[29] T. Taminiau *et al.* Detection and Control of Individual Nuclear Spins Using a Weakly Coupled Electron Spin. *Physical Review Letters* **109**, 137602 (2012).

[30] S. Kolkowitz, Q. P. Unterreithmeier, S. D. Bennett and M. D. Lukin. Sensing distant nuclear spins with a single electron spin. *Physical Review Letters* **109**, 137601 (2012).

[31] A. N. Jordan and A. N. Korotkov. Qubit feedback and control with kicked quantum nondemolition measurements: A Bayesian approach. *Phys. Rev. B* **74**, 085307 (2006).

[32] H. Bernien *et al.* Heralded entanglement between solid-state qubits separated by three metres. *Nature* **497**, 86 (2013).

[33] F. Dolde *et al.* Room-temperature entanglement between single defect spins in diamond. *Nature Physics* 139–143 (2013).

Chapter 5

# Heralded entanglement between solid-state qubits separated by three metres

H. Bernien, B. Hensen, W. Pfaff, G. Koolstra, M.S. Blok, L. Robledo, T.H. Taminiau, M. Markham, D.J. Twitchen, L. Childress, and R. Hanson

Quantum entanglement between spatially separated objects is one of the most intriguing phenomena in physics. The outcomes of independent measurements on entangled objects show correlations that cannot be explained by classical physics. Besides being of fundamental interest, entanglement is a unique resource for quantum information processing and communication. Entangled qubits can be used to establish private information or implement quantum logical gates [1,2]. Such capabilities are particularly useful when the entangled qubits are spatially separated [3,4,5], opening the opportunity to create highly connected quantum networks [6] or extend quantum cryptography to long distances [7,8]. Here we present a key experiment towards the realisation of long-distance quantum networks with solid-state quantum registers. We have entangled two electron spin qubits in diamond that are separated by a three-metre distance. We establish this entanglement using a robust protocol based on local creation of spin-photon entanglement and a subsequent joint measurement of the photons. Detection of the photons heralds the projection of the spin qubits onto an entangled state. We verify the resulting non-local quantum correlations by performing single-shot readout [9] on the qubits in different bases. The long-distance entanglement reported here can be combined with recently achieved initialisation, readout and entanglement operations [9,10,11,12,13] on local long-lived nuclear spin registers, enabling deterministic long-distance teleportation, quantum repeaters and extended quantum networks.

This chapter has been published in *Nature* **497**, 86 (2013).

## 5.1 Introduction

A quantum network can be constructed by using entanglement to connect local processing nodes, each containing a register of well-controlled and long-lived qubits [6]. Solids are an attractive platform for such registers, as the use of nano-fabrication and material design may enable well-controlled and scalable qubit systems [14]. The potential impact of quantum networks on science and technology has recently spurred research efforts towards generating entangled states of distant solid-state qubits [15,16,17,18,19,20,21].

A prime candidate for a solid-state quantum register is the nitrogen-vacancy (NV) defect centre in diamond. The NV centre combines a long-lived electronic spin (S=1) with a robust optical interface, enabling measurement and high-fidelity control of the spin qubit [15,22,23,24]. Furthermore, the NV electron spin can be used to access and manipulate nearby nuclear spins [9,10,11,12,13], thereby forming a multi-qubit register. To use such registers in a quantum network requires a mechanism to coherently connect remote NV centres.

Here we demonstrate the generation of entanglement between NV centre spin qubits in distant setups. We achieve this by combining recently established spin initialisation and single-shot readout techniques [9] with efficient resonant optical detection and feedback-based control over the optical transitions, all in a single experiment and executed with high fidelity. These results put solid-state qubits on par with trapped atomic qubits [3,4,5] as highly promising candidates for implementing quantum networks.

Our experiment makes use of two NV spin qubits located in independent low-temperature setups separated by 3 metres (Fig. 5.1a). We encode the qubit basis states $|\uparrow\rangle$ and $|\downarrow\rangle$ in the NV spin sub-levels $m_\mathrm{s} = 0$ and $m_\mathrm{s} = -1$, respectively. Each qubit can be independently read out by detecting spin-dependent fluorescence in the NV phonon side band (non-resonant detection) [9]. The qubits are individually controlled with microwave pulses applied to on-chip strip-lines [23]. Quantum states encoded in the qubits are extremely long-lived: using dynamical decoupling techniques [23] we obtain a coherence time exceeding 10 ms (Fig. ??), the longest coherence time measured to date for a single electron spin in a solid.

## 5.2 Protocol

We generate and herald entanglement between these distant qubits by detecting the resonance fluorescence of the NV centres. The specific entanglement protocol we employ is based on the proposal of S. Barrett and P. Kok [25], and is schematically drawn in figure ??b. Both centres NV A and NV B are initially prepared in a superposition $1/\sqrt{2}(|\uparrow\rangle + |\downarrow\rangle)$. Next, each NV centre is excited by a short laser pulse that is resonant with the $|\uparrow\rangle$ to $|e\rangle$ transition, where $|e\rangle$ is an optically excited state with the same spin projection as $|\uparrow\rangle$. Spontaneous emission locally entangles the qubit and photon number, leaving each setup in the state $1/\sqrt{2}(|\uparrow 1\rangle + |\downarrow 0\rangle)$, where 1 (0) denotes the presence (absence)

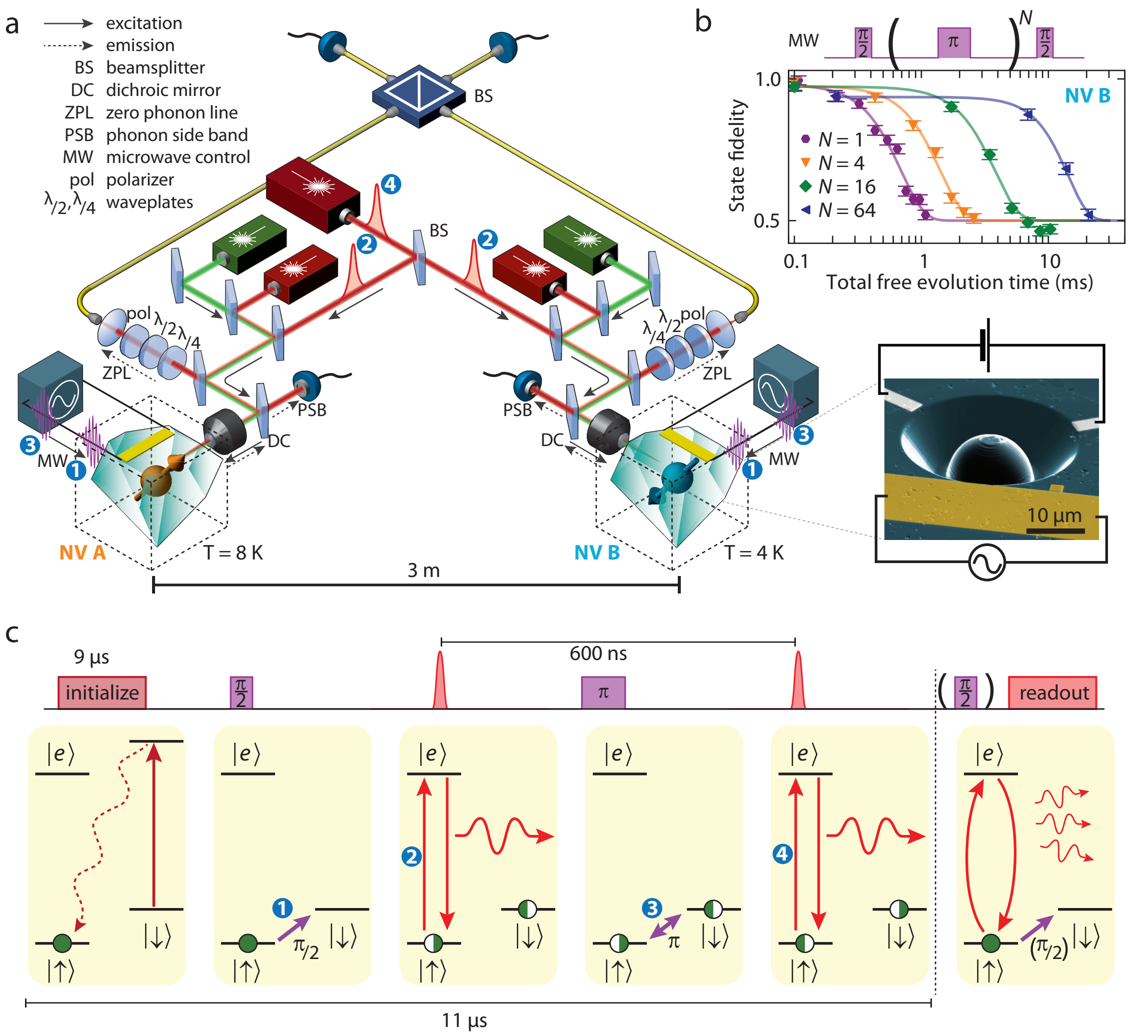


**Figure 5.1 | Experimental setup. a,** Each nitrogen vacancy (NV) centre resides in a synthetic ultra-pure diamond oriented in the $\langle 111 \rangle$ direction. The two diamonds are located in two independent low-temperature confocal microscope setups separated by 3 metres. The NV centres can be individually excited resonantly by a red laser and off-resonantly by a green laser. The emission (dashed arrows) is spectrally separated into an off-resonant part (phonon side band, PSB) and a resonant part (zero-phonon line, ZPL). The PSB emission is used for independent single-shot readout of the spin qubits[9]. The ZPL photons from the two NV centres are overlapped on a fiber-coupled beamsplitter. Microwave pulses for spin control are applied via on-chip microwave strip-lines. An applied magnetic field of 17.5 G splits the $m_s = \pm 1$ levels in energy. The optical frequencies of NV B are tuned by a d.c. electric field applied to the gate electrodes (**b,** scanning electron microscope image of a similar device). To enhance the collection efficiency, solid immersion lenses have been milled around the two NV centres[9].

of an emitted photon; the joint qubit-photon state of both setups is then described by $1/2(|{\uparrow_A}{\uparrow_B}\rangle\,|1_A 1_B\rangle + |{\downarrow_A}{\downarrow_B}\rangle\,|0_A 0_B\rangle + |{\uparrow_A}{\downarrow_B}\rangle\,|1_A 0_B\rangle + |{\downarrow_A}{\uparrow_B}\rangle\,|0_A 1_B\rangle)$. The two photon modes, A and B, are directed to the input ports of a beamsplitter (see Fig. 5.1a), so that fluorescence observed in an output port could have originated from either NV centre. If the photons emitted by the two NV centres are indistinguishable, detection of precisely one photon on an output port would correspond to measuring the photon state $|1_A 0_B\rangle \pm e^{-i\varphi}\,|0_A 1_B\rangle$ (where $\varphi$ is a phase that depends on the optical path length). Such a detection event would thereby project the qubits onto the maximally entangled state $|\psi\rangle = 1/\sqrt{2}(|{\uparrow_A}{\downarrow_B}\rangle \pm e^{-i\varphi}\,|{\downarrow_A}{\uparrow_B}\rangle)$.

Any realistic experiment, however, suffers from photon loss and imperfect detector efficiency; detection of a single photon is thus also consistent with creation of the state $|{\uparrow\uparrow}\rangle$. To eliminate this possibility, both qubits are flipped and optically excited for a second time. Since $|{\uparrow\uparrow}\rangle$ is flipped to $|{\downarrow\downarrow}\rangle$, no photons are emitted in the second round for this state. In contrast, the states $|\psi\rangle$ will again yield a single photon. Detection of a photon in both rounds thus heralds the generation of an entangled state. The second round not only renders the protocol robust against photon loss, but it also changes $\varphi$ into a global phase, making the protocol insensitive to the optical path length difference[25] (see Supporting Material). Furthermore, flipping the qubits provides a refocusing mechanism that counteracts spin dephasing during entanglement generation. The final state is one of two Bell states $|\psi^{\pm}\rangle = 1/\sqrt{2}(|{\uparrow_A}{\downarrow_B}\rangle \pm |{\downarrow_A}{\uparrow_B}\rangle)$, with the sign depending on whether the same detector (+), or different detectors (−) clicked in the two rounds.

## 5.3 Implementation

A key challenge for generating remote entanglement with solid-state qubits is obtaining a large flux of indistinguishable photons, in part because local strain in the host lattice can induce large variations in photon frequency. The optical excitation spectra of the NV centres (Fig. 5.2a) display sharp spin-selective transitions. Here we use the $E_y$ transition (spin projection $m_s = 0$) in the entangling protocol and for qubit readout; we use the $A_1$ transition for fast optical pumping into $|{\uparrow}\rangle$[9]. Due to different strain in the two diamonds, the frequencies of the $E_y$ transitions differ by 3.5 GHz, more than 100 line-widths. By applying a voltage to an on-chip electrode (Fig. 5.1b) we tune the optical transition frequencies of one centre (NV B) through the d.c. Stark effect[18,26] and bring the $E_y$ transitions of the two NV centres into resonance (Fig. 5.2a bottom).

Charge fluctuations near the NV centre also affect the optical frequencies. To counteract photo-ionisation we need to regularly apply a green laser pulse to re-pump the NV centre into the desired charge state. This re-pump pulse changes the local electrostatic environment, leading to jumps of several line-widths in the optical transition frequencies[27]. To overcome these effects, we only initiate an experiment if the number of photons collected during a two-laser probe stage (Fig. 5.2b) exceeds a threshold, thereby ensuring that the NV centre optical transitions are on resonance with the lasers (see chapter ??). The preparation

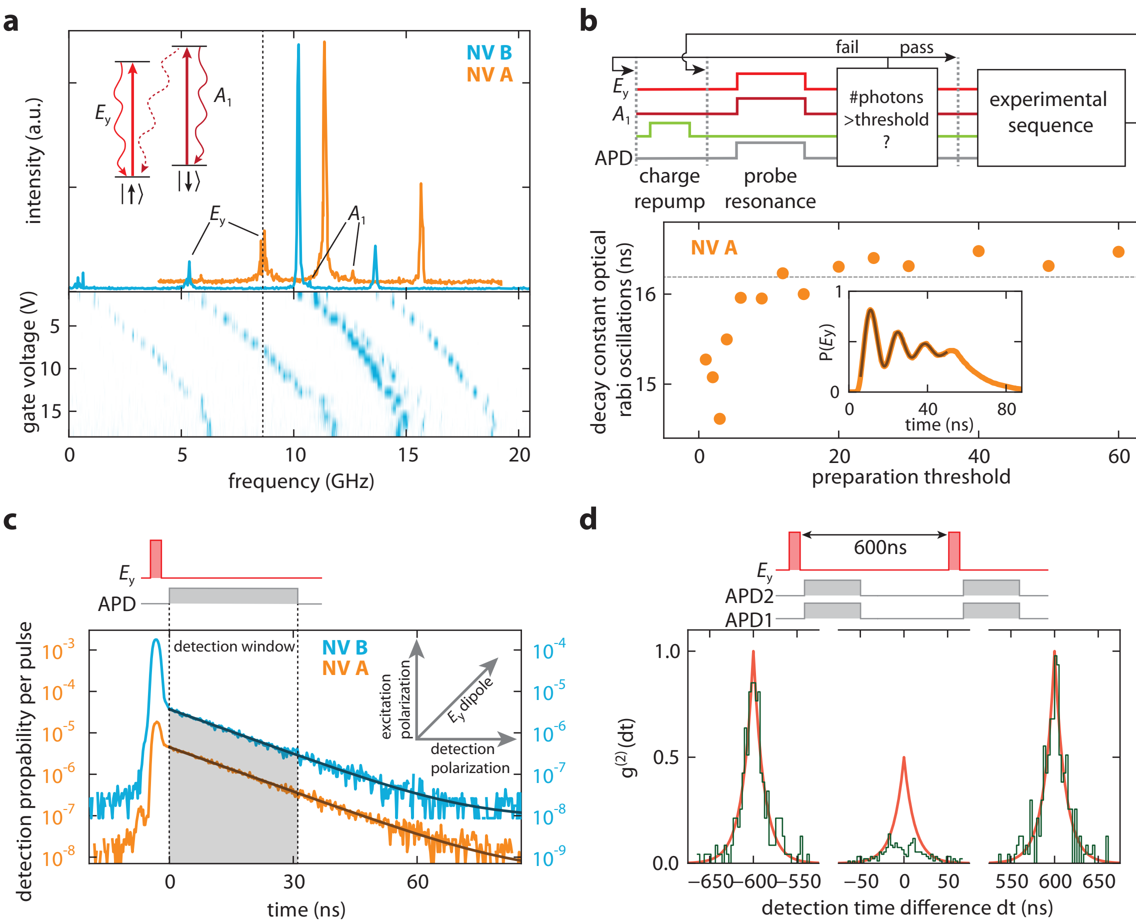


**Figure 5.2 | Generating and detecting indistinguishable photons. a,** Excitation spectra; frequency relative to 470.4515 THz. By applying a voltage to the gates of NV B the $E_y$ transitions are tuned into resonance. **b,** Dynamical preparation of charge and optical resonance. Top: Preparation protocol. A 10 $\mu$s green laser pulse pumps the NV into its negative charge state[9]. The transition frequencies are probed by exciting the $E_y$ and $A_1$ transitions for 60 $\mu$s. Conditional on surpassing a certain number of photons detected the experiment is started (pass) or preparation is repeated (fail). APD, avalanche photodiode. Bottom: Line-narrowing effect of the preparation shown by the dependence of the decay time of optical Rabi oscillations on preparation threshold. Dashed line indicates lifetime-limited damping[27]. **c,** Resonant optical excitation and detection. The polarisation axis of the detection path is aligned perpendicular to the excitation axis. The dipole axis of the $E_y$ transition is oriented in between these two axes (inset). Remaining laser light reflection is time-filtered by defining a photon detection window that starts after the laser pulse. **d,** Two-photon quantum interference using resonant excitation and detection. The $g^{(2)}$ correlation function is obtained from all coincidence detection events of APD 1 and APD 2 during the entanglement experiment (see Supporting Material). The side-peaks are fit to an exponential decay; from the fit values, we obtain the expected central peak shape $g^{(2)}_{\perp}$ (red line) for non-interfering photons. The visibility of the interference is given by $(g^{(2)}_{\perp} - g^{(2)})/g^{(2)}_{\perp}$.

procedure markedly improves the observed optical coherence: as the probe threshold is increased, optical Rabi oscillations persist for longer times (see Fig. 5.2b). For high thresholds, the optical damping time saturates around the value expected for a lifetime-limited linewidth[27], indicating that the effect of spectral jumps induced by the re-pump laser is strongly mitigated.

Besides photon indistinguishability, successful execution of the protocol also requires that the detection probability of resonantly emitted photons exceeds that of scattered laser photons and of detector dark counts. This is particularly demanding for NV centres since only about 3% of their emission is in the zero-phonon line and useful for the protocol. To minimise detection of laser photons, we use both a cross-polarised excitation-detection scheme (Fig. 5.2c inset) and a detection time filter that exploits the difference between the length of the laser pulse (2 ns) and the NV centre's excited state lifetime (12 ns) (Fig. 5.2c). For a typical detection window used, this reduces the contribution of scattered laser photons to about 1%. Combined with micro-fabricated solid-immersion lenses for enhanced collection efficiency (Fig. 5.1b) and spectral filtering for suppressing non-resonant NV emission, we obtain a detection probability of a resonant NV photon of about $4 \times 10^{-4}$ per pulse — about 70 times higher than the sum of background contributions.

The degree of photon indistinguishability and background suppression can be obtained directly from the second-order autocorrelation function $g^{(2)}$, which we extract from our entanglement experiment (see Supporting Material). For fully distinguishable photons, the value of $g^{(2)}$ would reach 0.5 at zero arrival time difference. A strong deviation from this behaviour is observed (Fig. 5.2d) due to two-photon quantum interference[28] that, for perfectly indistinguishable photons, would make the central peak fully vanish. The remaining coincidences are likely caused by (temperature-dependent) phonon-induced transitions between optically excited states[29] in NV A. The visibility of the two-photon interference observed here — $(80 \pm 5)$% for $|dt| < 2.56$ ns — is a significant improvement over previously measured values[18,19] and key to the success of the entangling scheme.

To experimentally generate and detect remote entanglement, we run the following sequence: First, both NV centres are independently prepared into the correct charge state and brought into optical resonance according to the scheme in figure 5.2b. Then we apply the entangling protocol shown in figure **??** using a 600 ns delay between the two optical excitation rounds. We repeat the protocol 300 times before we return to the resonance preparation step; this number is a compromise between maximising the attempt rate and minimising the probability of NV centre ionisation. A fast logic circuit monitors the photon counts in real time and triggers single-shot qubit readout on each setup whenever entanglement is heralded, i.e. whenever a single photon is detected in each round of the protocol. The readout projects each qubit onto the $\{|\uparrow\rangle, |\downarrow\rangle\}$ states (Z-basis), or on the $\{|\uparrow\rangle \pm |\downarrow\rangle, |\uparrow\rangle \mp |\downarrow\rangle\}$ states (X or $-$X basis). The latter two are achieved by first rotating the qubit by $\pi/2$ using a microwave pulse before readout. By correlating the resulting single-qubit readout outcomes we can verify the generation of the desired entangled states. To obtain reliable estimates of the two-qubit state probabilities, we correct the raw data with a maximum-likelihood method for local readout infidelities. These readout errors are known accurately from regular calibrations performed during the experiment (see Supporting Material).

## 5.4 Results

Figure 5.3 shows the obtained correlations. When both qubits are measured along Z (readout basis {Z,Z}), the states $\psi^+$ and $\psi^-$ (as identified by their different photon signatures) display strongly anti-correlated readout results (odd parity). The coherence of the joint qubit state is revealed by measurements performed in rotated bases ({X,X}, {−X,X}), which also exhibit significant correlations. Furthermore, these measurements allow us to distinguish between states $\psi^+$ and $\psi^-$. For $\psi^+$ the {X,X} ({−X,X}), outcomes exhibit even (odd) parity, whereas the $\psi^-$ state displays the opposite behaviour, as expected. The observed parities demonstrate that the experiment yields the two desired entangled states.

We calculate a strict lower bound on the state fidelity by combining the measurement results from different bases (see Supporting Material):

$$F = \langle\psi^{\pm}|\rho|\psi^{\pm}\rangle \geq \ 1/2(P_{\uparrow\downarrow} + P_{\downarrow\uparrow} + C) - \sqrt{P_{\uparrow\uparrow}P_{\downarrow\downarrow}}, \tag{5.1}$$

where $P_{ij}$ is the probability for the measurement outcome $ij$ in the {Z,Z} basis (i.e. the diagonal elements of the density matrix $\rho$) and $C$ is the contrast between odd and even outcomes in the rotated bases. We find a lower bound of $(69 \pm 5)$% for $\psi^-$ and $(58 \pm 6)$% for $\psi^+$, and probabilities of 99.98% and 91.8%, respectively, that the state fidelity is above the classical limit of 0.5. These values firmly establish that we have created remote entanglement, and are the main result of this paper.

The lower bound on the state fidelity given above takes into account the possible presence of coherence within the even-parity subspace $\{|\uparrow\uparrow\rangle, |\downarrow\downarrow\rangle\}$. However, the protocol selects out states with odd parity and therefore this coherence is expected to be absent. To compare the results to the expected value and to account for sources of error, we set the related (square-root) term in Eq. 1 to zero and obtain for the data in figure 5.3 as best estimate $F = (73 \pm 4)$% for $\psi^-$ and $F = (64 \pm 5)\%$ for $\psi^+$.

Several known error sources contribute to the observed fidelity. Most importantly, imperfect photon indistinguishability reduces the coherence of the state. In figure 5.4a we plot the maximum state fidelity expected from photon interference data (Fig. 5.2d) together with the measured state fidelities, as a function of the maximum allowed difference in detection time of the two photons relative to their respective laser pulses. We find that the fidelity can be slightly increased by restricting the data to smaller time differences, albeit at the cost of a lower success rate (Fig. 5.4b).

The fidelity is further decreased by errors in the microwave pulses (estimated at 3.5%), spin initialisation (2%), spin decoherence ($< 1\%$) and spin flips during the optical excitation (1%) (see Supporting Material). Moreover, $\psi^+$ is affected by after-pulsing, whereby detection

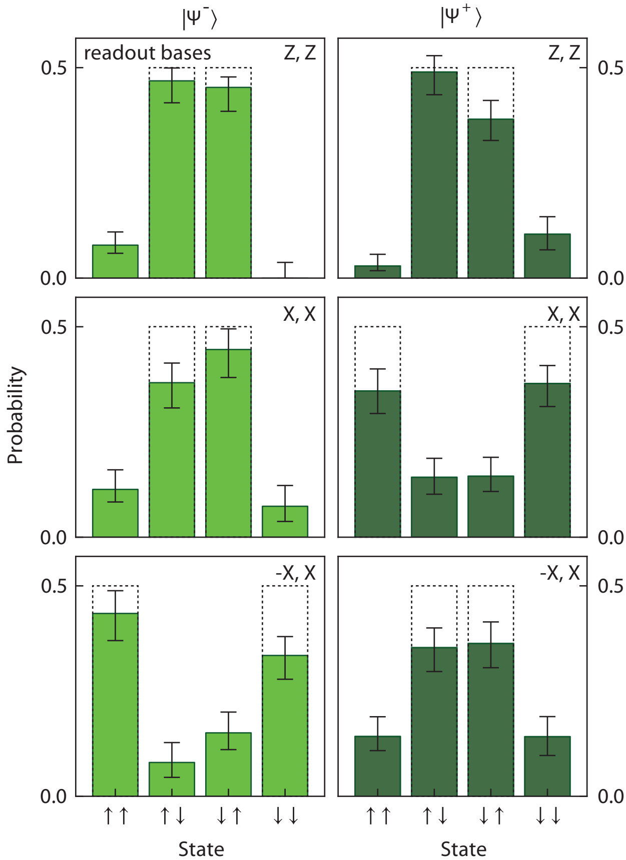


**Figure 5.3 | Verification of entanglement by spin-spin correlations.** Each time that entanglement is heralded the spin qubits are individually read out and their results correlated. The readout bases for NV A and NV B can be rotated by individual microwave control (see text). The state probabilities are obtained by a maximum-likelihood estimation on the raw readout results (see Supporting Material). Error bars depict 68% confidence intervals; dashed lines indicate expected results for perfect state fidelity. Data is obtained from 739 heralding events. For $\psi^-$, the detection window in each round is set to 38.4 ns, and the maximum absolute detection time difference $|\delta\tau|$ between the two photons relative to their laser pulses is restricted to 25.6 ns. $\delta\tau = \tau_2 - \tau_1$, where $\tau_1$ is the arrival time of the first photon relative to the first laser pulse and $\tau_2$ the arrival time of the second photon relative to the second laser pulse. For $\psi^+$ the second detection window is set to 19.2 ns with $|\delta\tau| < 12.8$ ns, in order to reduce the effect of photo-detector after-pulsing.

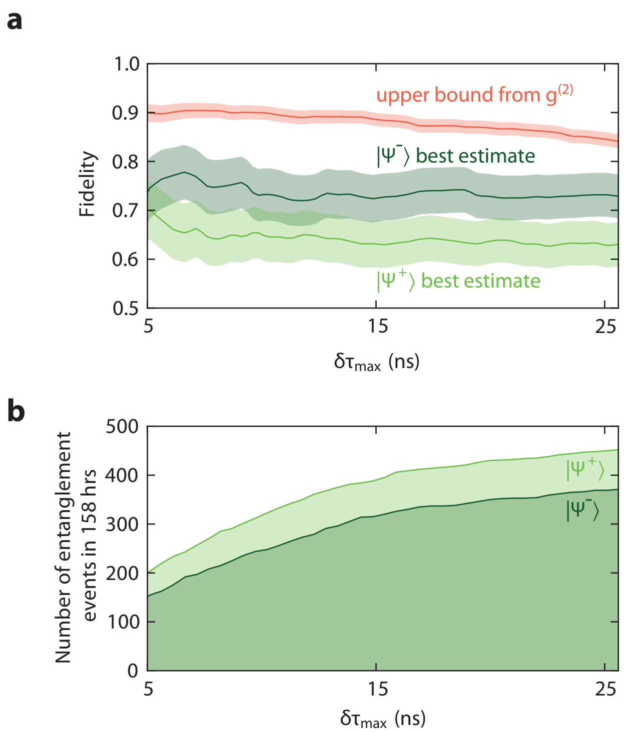


**Figure 5.4 | Dependence of the fidelity and number of entanglement events on the detection time difference of the photons.** **a,** Upper bound on the state fidelity from photon interference data (see Supporting Material) and best estimate of the state fidelity from the correlation data as a function of the maximum allowed photon detection time difference ($|\delta\tau| < \delta\tau_{\mathrm{max}}$). Detection time windows are chosen as in figure 5.3. Shaded regions indicate 68% confidence intervals. **b,** Number of entanglement events obtained during 158 hours as a function of the maximum allowed photon detection time difference $\delta\tau_{\mathrm{max}}$.

of a photon in the first round triggers a fake detector click in the second round. Such afterpulsing leads to a distortion of the correlations (see for example the increased probability for $|\downarrow\downarrow\rangle$ in figure 5.3) and thereby a reduction in fidelity for $\psi^+$ (see Supporting Material). Besides these errors that reduce the actual state fidelity, the measured value is also slightly lowered by a conservative estimation for readout infidelities and by errors in the final microwave $\pi/2$ pulse used for reading out in a rotated basis.

The fidelity of the remote entanglement can be significantly increased in future experiments by further improving photon indistinguishability. This may be achieved by more stringent frequency selection in the resonance initialisation step and by working at lower temperatures, which will reduce phonon-mediated excited-state mixing[29]. Also, the microwave errors can be much reduced; for instance by using isotopically purified diamonds[12] and polarising the host nitrogen nuclear spin[9].

The success probability of the protocol is given by $P_\psi = 1/2\eta_A\eta_B$. $\eta_i$ is the overall detection efficiency of resonant photons from NV $i$ and the factor 1/2 takes into account cases where the two spins are projected into $|\downarrow\downarrow\rangle$ or $|\uparrow\uparrow\rangle$, which are filtered out by their different photon signature. In the current experiment we estimate $P_\psi \approx 10^{-7}$ from the data in figure 5.4c. The entanglement attempt rate is about 20 kHz, yielding one entanglement event per 10 minutes. This is in good agreement with the 739 entanglement events obtained over a time of 158 hours. The use of optical cavities will greatly enhance both the collection efficiency and emission in the zero-phonon line[30] and increase the success rate by several orders of magnitude.

## 5.5 Conclusion

Creation of entanglement between distant spin qubits in diamond, as reported here, opens the door to extending the remarkable properties of NV-based quantum registers towards applications in quantum information science. By transferring entanglement to nuclear spins near each NV centre, a nonlocal state might be preserved for seconds or longer[12], facilitating the construction of cluster states[2] or quantum repeaters[8]. At the same time, the auxiliary nuclear spin qubits also provide an excellent resource for processing and error correction. When combined with future advances in nanofabricated integrated optics and electronics, the use of electrons and photons as quantum links and nuclear spins for quantum processing and memory offers a compelling route towards realization of solid-state quantum networks.

## 5.6 Bibliography

[1] M. A. Nielsen and I. L. Chuang. *Quantum Computation and Quantum Information.* Cambridge University Press (2000).

[2] R. Raussendorf and H. J. Briegel. A One-Way Quantum Computer. *Phys. Rev. Lett.* **86**, 5188 (2001).

[3] D. L. Moehring *et al.* Entanglement of single-atom quantum bits at a distance. *Nature* **449**, 68 (2007).

[4] S. Ritter *et al.* An elementary quantum network of single atoms in optical cavities. *Nature* **484**, 195 (2012).

[5] J. Hofmann *et al.* Heralded Entanglement Between Widely Separated Atoms. *Science* **337**, 72 (2012).

[6] H. J. Kimble. The quantum internet. *Nature* **453**, 1023 (2008).

[7] L. M. Duan, M. D. Lukin, J. I. Cirac and P. Zoller. Long-distance quantum communication with atomic ensembles and linear optics. *Nature* **414**, 413 (2001).

[8] L. Childress, J. M. Taylor, A. S. Sørensen and M. D. Lukin. Fault-Tolerant Quantum Communication Based on Solid-State Photon Emitters. *Phys. Rev. Lett.* **96**, 070504 (2006).

[9] L. Robledo *et al.* High-fidelity projective read-out of a solid-state spin quantum register. *Nature* **477**, 574 (2011).

[10] P. Neumann *et al.* Single-Shot Readout of a Single Nuclear Spin. *Science* **329**, 542 (2010).

[11] P. Neumann *et al.* Multipartite Entanglement Among Single Spins in Diamond. *Science* **320**, 1326 (2008).

[12] P. C. Maurer *et al.* Room-Temperature Quantum Bit Memory Exceeding One Second. *Science* **336**, 1283 (2012).

[13] W. Pfaff *et al.* Demonstration of entanglement-by-measurement of solid-state qubits. *Nature Physics* **9**, 29 (2013).

[14] T. D. Ladd *et al.* Quantum computers. *Nature* **464**, 45 (2010).

[15] E. Togan *et al.* Quantum entanglement between an optical photon and a solid-state spin qubit. *Nature* **466**, 730 (2010).

[16] W. B. Gao, P. Fallahi, E. Togan, J. Miguel-Sanchez and A. Imamoglu. Observation of entanglement between a quantum dot spin and a single photon. *Nature* **491**, 426 (2012).

[17] K. De Greve *et al.* Quantum-dot spin–photon entanglement via frequency downconversion to telecom wavelength. *Nature* **491**, 421 (2012).

[18] H. Bernien *et al.* Two-Photon Quantum Interference from Separate Nitrogen Vacancy Centers in Diamond. *Phys. Rev. Lett.* **108**, 043604 (2012).

[19] A. Sipahigil *et al.* Quantum Interference of Single Photons from Remote Nitrogen-Vacancy Centers in Diamond. *Phys. Rev. Lett.* **108**, 143601 (2012).

[20] R. B. Patel *et al.* Two-photon interference of the emission from electrically tunable remote quantum dots. *Nature Photon.* **4**, 632 (2010).

[21] E. B. Flagg *et al.* Interference of Single Photons from Two Separate Semiconductor Quantum Dots. *Phys. Rev. Lett.* **104**, 137401 (2010).

[22] G. D. Fuchs, V. V. Dobrovitski, D. M. Toyli, F. J. Heremans and D. D. Awschalom. Gigahertz Dynamics of a Strongly Driven Single Quantum Spin. *Science* **326**, 1520 (2009).

[23] G. de Lange, Z. H. Wang, D. Ristè, V. V. Dobrovitski and R. Hanson. Universal Dynamical Decoupling of a Single Solid-State Spin from a Spin Bath. *Science* **330**, 60 (2010).

[24] T. van der Sar *et al.* Decoherence-protected quantum gates for a hybrid solid-state spin register. *Nature* **484**, 82 (2012).

[25] S. D. Barrett and P. Kok. Efficient high-fidelity quantum computation using matter qubits and linear optics. *Phys. Rev. A* **71**, 060310 (2005).

[26] L. C. Bassett, F. J. Heremans, C. G. Yale, B. B. Buckley and D. D. Awschalom. Electrical Tuning of Single Nitrogen-Vacancy Center Optical Transitions Enhanced by Photoinduced Fields. *Phys. Rev. Lett.* **107**, 266403 (2011).

[27] L. Robledo, H. Bernien, I. van Weperen and R. Hanson. Control and Coherence of the Optical Transition of Single Nitrogen Vacancy Centers in Diamond. *Phys. Rev. Lett.* **105**, 177403 (2010).

[28] C. K. Hong, Z. Y. Ou and L. Mandel. Measurement of subpicosecond time intervals between two photons by interference. *Phys. Rev. Lett.* **59**, 2044 (1987).

[29] K.-M. C. Fu *et al.* Observation of the Dynamic Jahn-Teller Effect in the Excited States of Nitrogen-Vacancy Centers in Diamond. *Phys. Rev. Lett.* **103**, 256404 (2009).

[30] I. Aharonovich, A. D. Greentree and S. Prawer. Diamond photonics. *Nature Photon.* **5**, 397 (2011).

[31] J. K. Lindsey. *Parametric Statistical Inference.* Clarendon Press, Oxford, UK (1996).

[32] H. K. Cummins, G. Llewellyn and J. A. Jones. Tackling systematic errors in quantum logic gates with composite rotations. *Phys. Rev. A* **67**, 42308 (2003).

[33] L. Childress *et al.* Coherent dynamics of coupled electron and nuclear spin qubits in diamond. *Science* **314**, 281 (2006).

[34] T. Gullion, D. B. Baker and M. S. Conradi. New, compensated carr-purcell sequences. *J. Magn. Reson.* **89**, 479 (1990).

[35] T. Legero, T. Wilk, A. Kuhn and G. Rempe. Characterization of Single Photons Using Two-Photon Interference. M. O. Scully and G. Rempe (editors), *Advances In Atomic, Molecular, and Optical Physics*, Academic Press, 253–289 (2006).